A High Fidelity, Computationally Efficient Transient Model of Interior Permanent Magnet Machine with Stator Turn Fault

Bhaskar Sen, *Student Member, IEEE*, Jiabin Wang, *Senior Member, IEEE*, and Panagiotis Lazari, *Student Member, IEEE*

***Abstract*— An accurate transient model of Interior Permanent Magnet (IPM) machine with stator turn fault with due account of magnetic saturation is essential to develop robust and sensitive inter-turn fault detection algorithms and to evaluate drive controller performance and stability under fault conditions. The paper proposes a general method of modeling stator turn fault using flux-linkage map of IPM machine under fault extracted from Finite Element (FE) analysis. Simulation results from the proposed fault model are compared against FE and experimental results. The results show that the proposed model matches well with experimental data.**

***Index Terms*— Fault currents, analytical models, permanent magnet machines, saturation magnetization, condition monitoring.**

NOMENCLATURE

i_d	*d*-axis current
i_q	*q*-axis current
i_f	fault current
λ_d	*d*-axis flux linkage
λ_q	*q*-axis flux linkage
μ	fault fraction
p	Number of pole pairs
R_s	Stator phase resistance
R_f	External fault resistance
L_{ls}	Stator leakage inductance
L_F	Faulted turn leakage inductance
V_d	*d*-axis voltage
V_q	*q*-axis voltage
θ_e , θ_{elect}	Rotor angle (electrical) w.r.t to phase A winding
θ_m, θ_{mech}	Rotor angle (mechanical) w.r.t to phase A winding
ω_e	Angular speed in rad/sec (electrical)
l_{stk}	*S*tator stack length
β	Skew angle (mechanical)
n	Number of skew slices of rotor
g	General nonlinear mapping function between flux-linkage/ torque to stator currents.

Manuscript received October 19, 2014; revised February 4, 2015 and August 2, 2015; accepted August 9, 2015.

This work was supported in part by the European ENIAC Joint Undertaking under the MotorBrain project.

The authors are with the Electrical Machines and Drives Research Group, Department of Electronic and Electrical Engineering, The University of Sheffield, Sheffield, S1 3JD, UK (email: elp11bs@sheffield.ac.uk).

I. INTRODUCTION

INTERIOR permanent magnet (IPM) machines are increasing being favored as the machine of choice for electric vehicle application due to their high power density, robustness, large constant power speed range and overall high efficiency [1]–[6]. However, due to presence of magnets in the rotor, electrical faults must be quickly detected and mitigating controls initiated to prevent catastrophic failure of the machine. Such a functionality commonly known as "limp-home" mode [7] is essential for providing high degree of availability, and reliability demanded in safety critical application such as electric vehicles. In order to develop sensitive fault detection algorithms and fault tolerant control strategies, an accurate transient model of the machine under fault condition is indispensable [8]–[10] at development stage in order to save time and resources spent on experimental testing. This is because many faults such as inter-turn short-circuit may cause benign changes in terminal voltages and currents. Consequently, it is difficult to detect them in an electrically noisy environment. Inaccurate representation of fault behaviors may lead to a detection algorithm working well in simulations, but not effective in real testing.

Several surveys on reliability of industrial motors conducted by Electric Power Research Institute EPRI [11] and IEEE [12]–[15] concluded that stator winding failures accounts for about 21-37% of faults in electrical machines. One of the leading causes of winding failure are inter-turn short-circuit failures which are especially critical, since it leads to a large circulating current in the faulted turns [16]. This gives rise a local hot spot which can cause further insulation failures and ultimately leading to a complete failure of the winding as a phase-ground or phase-to-phase fault [17]. The large circulating current in the faulted turns can also produce irreversible demagnetization of the magnets [18].

The modeling of inter-turn short-circuit fault in IPM was treated in [19], where a phase variable model of IPM motor under condition of linear magnetic characteristics was derived, by extending the fault model derived for induction motors in

[20]. However, no experimental validation was reported. In [21] a method of extending the IPM model under fault accounting for magnetic saturation was proposed. The self- and mutual-fluxes of the healthy and faulted turns are assumed to be proportional to their number of turns. The phase inductance variation due to saturation described in [21] is obtained by computing first the saturated values of *d*- and *q*-axis inductances, L_d, and L_q, and then performing inverse transformation to *abc* quantities. However, this assumption is not strictly true for most PM machines in which a significant part of the self- and mutual-inductances is contributed by the slot leakage. Moreover, the concept was not tested in simulation or experiments. In [8], [22], [23] an FE time stepping co-simulation transient model of BLDC was used for developing fault detection algorithms. However, time stepped FE simulation is very time consuming and not suitable for computationally efficient simulation studies involving pulse-width modulated (PWM) drives, due to the small time scales involved. Moreover, in case of IPM machine, fault detection needs to be tested at a number of different *dq* currents due to magnetic non-linearity, which will further increase compute time. In [24], [25], a fault model for IPM BLDC was derived using winding function theory (WFT) for single layer magnet rotor, neglecting magnetic saturation effects. The inverse air gap function used in [25] is difficult to derive for more complex rotor geometries common in high saliency machines. In [26] a permeance network (PN) model for turn faults in saturated PMSMs was proposed. The permeance network model is then used to extract 4-dimensional (4-d) flux/inductance lookup tables needed to formulate the transient model. However no experimental validation was performed. Further derivation of a PN model is very tedious, and compromises accuracy, especially for complex rotor geometries. In [10] and [27] an inductance based model was proposed for inter-turn fault detection in PM synchronous machines. However, IPM machines with buried magnets exhibits high level of magnetic saturation and cross-saturation effects and therefore separation of armature reaction flux linkage from the total flux linkage will incur large error and hence compromises model accuracy [28]–[33]. Moreover the method of extraction of inductances reported in [27] and [34] by energy-perturbation is computationally more demanding requiring twice as many FE computations [32]. A hybrid model for wound-rotor synchronous generator reported in [35] assumes that the machine operates in linear region under healthy condition. However, this assumption is not applicable to IPM machines with high level of magnetic saturation [32].

The aim of this paper is to establish an accurate and computationally efficient model of IPM machines under stator turn fault. This is achieved by extracting flux linkage map of the machine under turn fault conditions using offline static FE analysis and combining it with voltage equations of the machine. The method is not limited to IPM machines and the same technique can be used for modeling stator turn faults in passive rotor systems including surface PM machines, switched reluctance machines, switched flux machines and, separately excited machines, such as wound field synchronous machines. This approach enables the full representation of spatial harmonics and magnetic saturation under inter-turn fault and all load conditions and therefore is the most accurate representation of the faulted motor behavior apart from a time stepping FE-coupled analysis [36]. Although the generation of flux map from offline static FE model is computationally expensive, once the lookup tables are established it will have a much faster simulation speed compared to time stepping FE coupled simulation [36]. This is quite advantageous in drive coupled simulation, since the PWM pulses are of small duration, an FE-coupled time stepping simulation is prohibitively expensive in terms of compute time. This method is also advantageous when numerous test cases under different loads and speeds need to be performed quickly during development of fault detection/mitigation schemes. Simplified models such as that presented in [19], [25] will not be able to represent the phenomena correctly over all load/speed ranges. It also allows speedup of simulation time compared to FE coupled simulation in case where the rotor is skewed, since multi-slice FE simulation has to perform simulation for all the skew slices which results in significant increase in the overall computation time [37]. It should also be noted that although it is possible to neglect saturation characteristics for simulation of turn fault as suggested by some authors [19], [25], the fault model thus obtained will not be useful to check validity of performance of fault detection and fault tolerant algorithms over the entire range of operation of the machine. This may lead to over-simplified fault detection and mitigation methods which work well with the simplified motor model, but may not perform well in actual test conditions. Extensive experimental tests are performed to validate the model over speed and load ranges.

II. Proposed Fault Model

It is well known that in order to accurately model behavior of a healthy IPM machine, a mapping of flux-linkages to current is needed [38], [28]. This non-linear flux linkage map can capture most of the behavior of the machine including the magnetic saturation, spatial saliency and harmonics [28]–[31]. 3-dimensional (3d) effects such as overhang fringe fields, iron losses and rotor eddy currents may also be included. Using the same approach, a model of a machine under stator turn fault can also be extracted using appropriate flux-linkage lookup tables together with voltage governing equations and loss components.

Without loss of generality, the turn fault is assumed to be in 'c' phase winding which is therefore divided into two sub-windings. Sub-winding 'cs1' is the healthy part and sub-winding 'cs2' is the faulty part as shown in Fig. 1. 'μ' represents the fault winding fraction, defined as the ratio of number of short-circuited turns in phase c (N_f) to the total number of turns in phase c (N_t) [19]. R_f represents the fault resistance, i_f denotes the current into the fault resistance.

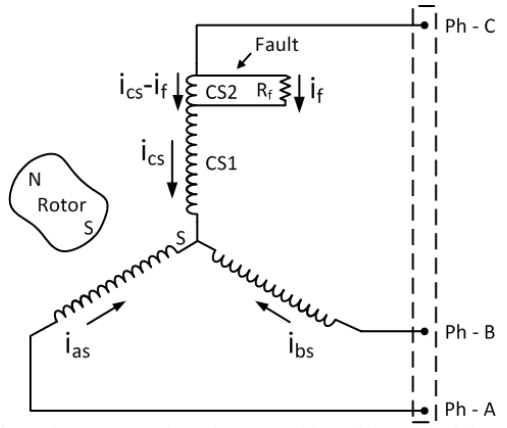

Fig. 1: Schematic representation of IPM machine with turn fault in 'C' phase.

A. Machine Equations in abc Frame

The stator equations for IPM machines with turn fault can be expressed as (1).

$$\boldsymbol{V_s}^{\boldsymbol{f}} = \boldsymbol{R_s}^{\boldsymbol{f}} \boldsymbol{i_s}^{\boldsymbol{f}} + d\boldsymbol{\lambda_s}^{\boldsymbol{f}} / dt \tag{1}$$

where,

$$\begin{aligned} \boldsymbol{V_s}^{\boldsymbol{f}} &= \left[v_{as} \quad v_{bs} \quad v_{cs1} \quad \left(v_{cs2} = v_f \right) \right]^T \\ \boldsymbol{i_s}^{\boldsymbol{f}} &= \left[i_{as} \quad i_{bs} \quad i_{cs} \quad i_{cs} - i_f \right]^T \\ \boldsymbol{\lambda_s}^{\boldsymbol{f}} &= \left[\lambda_{as} \quad \lambda_{bs} \quad \lambda_{cs1} \quad \left(\lambda_{cs2} = \lambda_f \right) \right]^T \\ \boldsymbol{R_s}^{\boldsymbol{f}} &= R_s \, diag\left[1 \quad 1 \quad 1-\mu \quad \mu \right]. \end{aligned} \tag{2}$$

Since IPM machine exhibits strong saturation, the flux linkage and torque is a nonlinear function of current and mechanical angular position. This relationship is denoted using function '*g*' as a general non-linearity function between the quantities as shown in,

$$\begin{aligned} \lambda_{xs} &= g_x \left(i_a, i_b, i_c, i_f, \theta_m \right) \\ T_e &= g_e \left(i_a, i_b, i_c, i_f, \theta_m \right) \end{aligned} \tag{3}$$

where, *x* denotes healthy phases *a*, *b*, and two sub-windings *cs1* or *cs2*(*f*) in phase *c*. Since terminal voltage of phase '*c*' is the sum of voltages of sub-winding '*cs1*' and '*cs2*', the last two rows of voltage equation in (2) can be added and re-arranged to obtain terminal voltages as shown by (4).

$$\boldsymbol{V_s} = R_s \boldsymbol{i_s} + \frac{d\boldsymbol{\lambda_s}}{dt} + \mu \boldsymbol{A_1} i_f \tag{4}$$

where,

$$\begin{aligned} \boldsymbol{V_s} &= \left[v_{as} \quad v_{bs} \quad \left(v_{cs} = v_{cs1} + v_{cs2} \right) \right]^T \\ \boldsymbol{i_s} &= \left[i_{as} \quad i_{bs} \quad i_{cs} \right]^T \\ \boldsymbol{\lambda_s} &= \left[\lambda_{as} \quad \lambda_{bs} \quad \left(\lambda_{cs} = \lambda_{cs1} + \lambda_{cs2} \right) \right]^T \\ \boldsymbol{A_1} &= -\left[0 \quad 0 \quad R_s \right]^T \end{aligned} \tag{5}$$

The voltage of the shorted winding '*cs2*' can be written separately as (6).

$$V_f = V_{cs2} = R_f i_f = \mu R_s \left(i_{cs} - i_f \right) + \frac{d\lambda_f}{dt} \tag{6}$$

Table I
SPECIFICATIONS AND DESIGN PARAMETERS OF THE MACHINE

Quantity	Unit	Value
Peak torque	Nm	30
Rated torque	Nm	17
Base Speed	r/min	2100
Max Speed	r/min	8200
Peak power	kW	6.6
Rated power	kW	3.75
Peak current	A	85
Number of pole-pairs	--	3
Number of slots	--	36
Active stack length	mm	105
Stator outer diameter	mm	120
Airgap	mm	0.35
Rotor diameter	mm	67
Rotor skew slices	--	3

B. Machine Equations in dq Frame

The stator equations can be transformed to the *dq* frame using the synchronous frame transformation defined in [39] to obtain (7).

$$\begin{aligned} \boldsymbol{V_{dq}} = \boldsymbol{R_s} \boldsymbol{i_{dq}} + d\boldsymbol{\lambda_{dq}} / dt + \omega_e \left[-\lambda_q \quad \lambda_d \right]^T \\ -\mu \frac{2}{3} R_s \left[\sin\left(\theta_e + 2\pi/3 \right) \quad \cos\left(\theta_e + 2\pi/3 \right) \right]^T i_f \end{aligned} \tag{7}$$

where,

$$\begin{aligned} \lambda_d &= g_d \left(i_d, i_q, i_f, \theta_m \right) \\ \lambda_q &= g_q \left(i_d, i_q, i_f, \theta_m \right) \end{aligned} \tag{8}$$

The voltage of the shorted turns can be expressed in terms of the *dq* currents as (9).

$$V_f = R_f i_f = \mu R_s \begin{pmatrix} i_d \sin\left(\theta_e + 2\pi/3 \right) \\ + i_q \cos\left(\theta_e + 2\pi/3 \right) - i_f \end{pmatrix} + \frac{d\lambda_f}{dt} \tag{9}$$

where,

$$\lambda_f = \lambda_{cs2} = g_f \left(i_d, i_q, i_f, \theta_m \right) \tag{10}$$

The torque of the faulted machine can be calculated by a torque lookup table obtained from static FE using (11).

$$T_e = g_T \left(i_d, i_q, i_f, \theta_m \right) \tag{11}$$

In order to use the model in dynamic simulations, the equations can be written in its integral form [39] given by (12)-(14).

$$\boldsymbol{\lambda_{dq}} = \int \left(\begin{aligned} &\boldsymbol{V_{dq}} - \boldsymbol{R_s} \boldsymbol{i_{dq}} - \omega_e \left[-\lambda_q \quad \lambda_d \right]^T \\ &+ \mu \frac{2}{3} R_s \begin{bmatrix} \sin\left(\theta_e + 2\pi/3 \right) \\ \cos\left(\theta_e + 2\pi/3 \right) \end{bmatrix} i_f \end{aligned} \right) dt \tag{12}$$

$$\lambda_f = \int \left(R_f i_f - \mu R_s \begin{pmatrix} i_d \sin\left(\theta_e + 2\pi/3 \right) \\ + i_q \cos\left(\theta_e + 2\pi/3 \right) - i_f \end{pmatrix} \right) dt \tag{13}$$

where,

$$\begin{aligned} i_d &= g_d^{-1} \left(\lambda_d, \lambda_q, \lambda_f, \theta_m \right) \\ i_q &= g_q^{-1} \left(\lambda_d, \lambda_q, \lambda_f, \theta_m \right) \\ i_f &= g_f^{-1} \left(\lambda_d, \lambda_q, \lambda_f, \theta_m \right) \end{aligned} \tag{14}$$

Therefore, if the non-linear mapping of the *d*-, *q*-, and *f*-flux linkages to i_d, i_q, i_f and θ_m can be obtained using static FE calculations, it can be used with a differential-algebraic (DAE) capable solver, such as Saber [40] to obtain the solution. Alternatively the current to flux linkage map can be numerically inverted to obtain the inverse mapping functions (14) which can be used with an ordinary differential equation (ODE) solver [41].

By way of example, Fig. 2 shows schematic of the ODE solver based fault model established using the proposed technique. It should be noted that the temperature effect of the phase resistance can be accounted in the model.

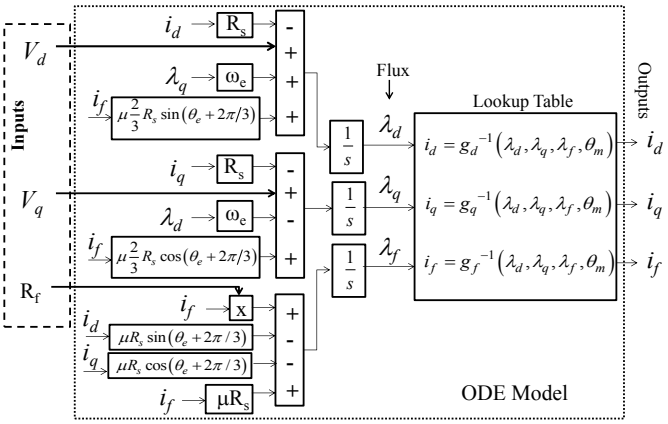

Fig. 2: Schematic of ODE solver based fault model.

C. FE model

For the purpose of validation of the proposed modeling methodology, an FE model of a 3-phase, 6-pole, 36-slot IPM motor with a two turn fault is generated. The machine is designed to maximize reluctance torque so that a high torque density can be achieved with low grade magnets, such as ferrite or bonded NdFeB. For this reason, it is often called permanent magnet assisted synchronous reluctance machine. The machine has 2 slots per pole per phase. The machine incorporates a 3-step rotor skew of 7º (mech). The main parameters of the machine are listed in Table I.

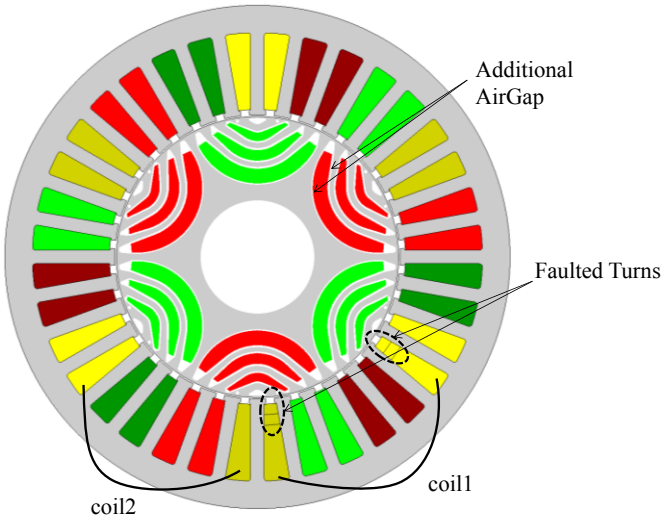

(a)

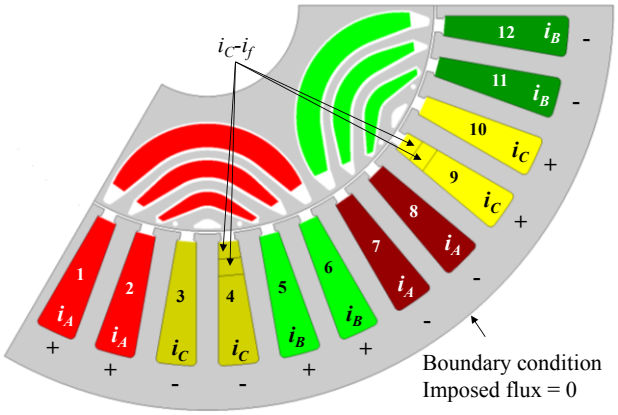

(b)

Fig. 3: FE model of 36 slot, 6 pole IPM Machine with 2 turn fault in C phase (a) full FE model, (b) zoomed portion of model containing turn fault showing excitation currents. (+, - signs depicts coil current direction. + represents current direction into the plane of the paper).

The laminations of the machine were manufactured by laser cutting and the damage to material property due to the cutting process [42] was accounted for in the FE model using additional air-gaps in the rotor. Fig. 3 shows the FE model including the two turn winding fault.

In order to obtain the flux-linkages map of the faulted machine for generating mode of operation magneto-static FE simulations are performed by varying i_q over [-70A, 10A], i_d over [-70A, 10A] in steps of 10A and i_f over [-350A, 350A] in steps of 50A over one complete electrical cycle [0, 120º] (mech). To cover both motoring and generating modes of operation, the corresponding d- and q-axis current range of [-70A, 70A] is necessary. Although the coarse steps of 50A for i_f may compromise accuracy of the flux linkage map it was selected to reduce the compute time. It is to be noted that in performing the FE simulations, the current in the 2 short-circuited turns are defined as i_c-i_f as illustrated in Fig. 1. The lookup tables needed in (8) and (10)-(11) can be obtained from FE simulations.

Although the faulted phase has been assumed to be in phase 'C', for the development of the model and for extraction of the flux linkage-current lookup tables, fault in any other phase can be simulated without the need to run any further FE computation, since fault in any other phase is simply a shift of electrical/mechanical angle. This can be achieved by modifying θ_e according to (15) and accordingly setting $\theta_m = \theta_e/p$ in the lookup tables.

$$\theta_e = \begin{cases} \theta_e - 2\pi/3 & ;\text{Phase A fault} \\ \theta_e - 4\pi/3 & ;\text{Phase B fault} \\ \theta_e & ;\text{Phase C fault} \end{cases} \quad (15)$$

D. Skew Computation

The machine selected for validation of fault modeling incorporates a rotor which consists of 3 identical rotor slices, which are skewed by -3.5º, 0º and +3.5º (mechanical). The rotor slices and shaft are shown in Fig. 11(b). The skewed rotor has slightly different current to flux linkage mapping compared to an un-skewed rotor and therefore needs to be accounted for in the modeling process. An accurate method to

model the effect of skew in healthy machines was presented in [37]. However, the method in [37] was shown to be valid for healthy machines and for machine with stator turn fault further refinement of the model needs to be performed. A general case of skew rotor slice is shown in Fig. 4 where, d_0, q_0 refers to the reference dq axis of the rotor with 0 skew angle, and d_s, q_s refer to the dq axis of the rotor with β mechanical skew angle.

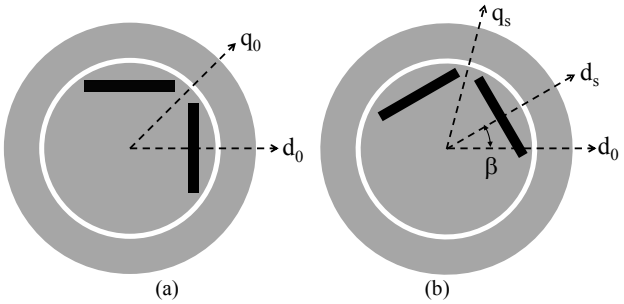

Fig. 4: Rotor skew slices at mechanical angle of (a) 0 (rad) skew, (b) β (rad) skew

Using the technique outlined in [37] the d-,q-, fault coil flux linkages and mechanical torque of any rotor slice skewed from the d_0- axis by an angle of β mechanical (rad) can be obtained by using modified dq currents in the lookup tables as shown in (16).

$$
\begin{aligned}
i_{ds} + ji_{qs} &= \left(i_d + ji_q\right)e^{-jp\beta} \\
\lambda_d + j\lambda_q &= \left\{\begin{matrix} g_d\left(i_{ds}, i_{qs}, i_f, \theta_m + \beta\right) \\ +jg_q\left(i_{ds}, i_{qs}, i_f, \theta_m + \beta\right)\end{matrix}\right\}e^{jp\beta} \\
\lambda_f &= g_f\left(i_{ds}, i_{qs}, i_f, \theta_m + \beta\right) \\
T_e\left(\theta_m\right) &= T_e\left(i_{ds}, i_{qs}, i_f, \theta_m + \beta\right)
\end{aligned}
\tag{16}
$$

where i_{ds} and i_{qs} are the d_s- and q_s- axis components of the stator current referred to the skewed d_s-q_s reference frame. The total flux-linkage and torque can be obtained by adding contribution of all the individual skewed rotor slices. In order to verify the proposed skew calculation technique, a test case of (i_d= -40A, i_q= -40A, i_f= -200A) was performed using multi-slice FE simulation and the proposed method, and the results are compared in Fig. 5.

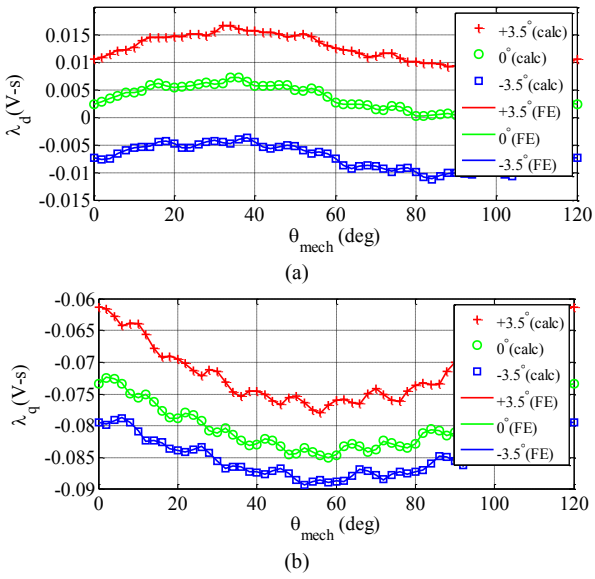

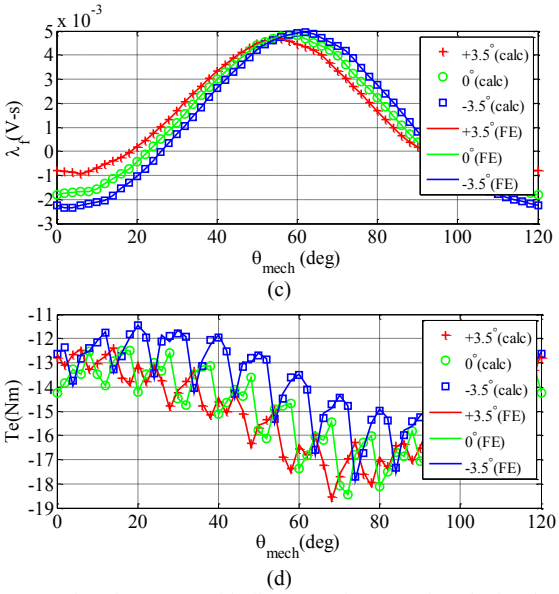

Fig. 5: Comparison between multi-slice FE and proposed method (calc) at (i_d= -40A, i_q= -40A, i_f= -200A) (a) d- axis flux linkage, (b) q- axis flux linkage, (c) faulted turn flux linkages (d) Torque

It can be seen from Fig. 5 that the match is excellent. This algorithm reduces the computation time by a factor of number of skew slices compared to performing static FE calculation for all rotor skew slices. This method is therefore used to generate the flux-linkage lookup tables.

III. Model Comparison

To illustrate the utility of ODE and DAE solvers for the proposed fault modeling approach without loss of generality, generator operation of the machine under study with a resistive load of 2.2Ω with two turn short-circuit fault at 3500 r/min and R_f=5.5mΩ is simulated by both the FE model and the proposed model implemented with the inverse lookup tables and ODE23s solver [41], and DAE solver [32]. It is to be noted that the FE and proposed models are simulated for 1 rotor slice in order to reduce FE computation time, and does not in any way affect model validation as long as the same current-flux linkage relation is maintained in the both models. Hardware validations provided in section IV uses the current-flux linkage map which accounts for the 3-step skewed rotor.

Fig. 6 and Fig. 7 show the comparison of FE predicted fault current and phase currents with those obtained from the ODE solver based model. As is quite evident the currents predicted by the proposed model matches very well with the FE results in terms of both peak and wave-shape.

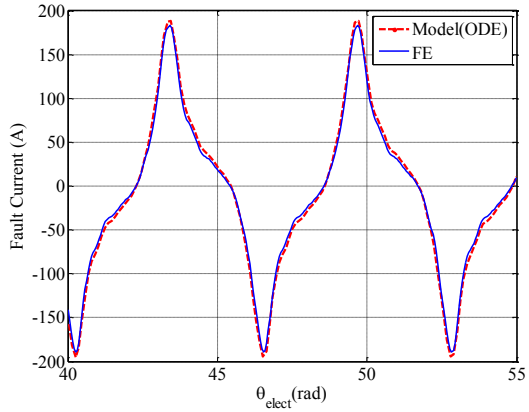

Fig. 6: Fault current comparison of FE verses model(ODE) solved by ODE solver at load of 2.2Ω at 3500 r/min

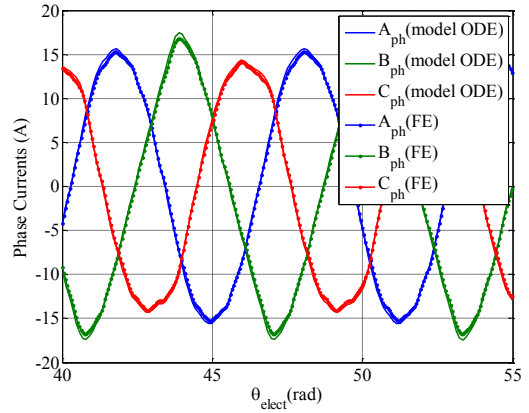

Fig. 7: Phase current comparison of FE verses model(ODE) solved by ODE solver at load of 2.2Ω at 3500 r/min

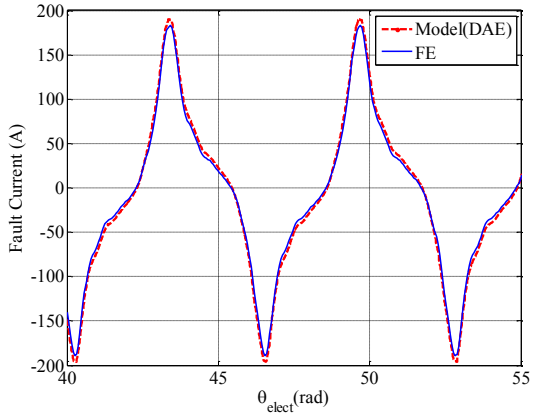

Fig. 8: Fault current comparison of FE verses model (DAE) solved by DAE solver at load of 2.2Ω at 3500 r/min

Table II
COMPARISON OF SIMULATION TIMES FOR GENERATOR MODE OPERATION WITH RESISTIVE LOAD OF 2.2Ω AT 3500 R/MIN

Method	Solution Time	Unit
FE	12420	s
ODE solver	62	s
DAE solver	78	s

Fig. 8 compares the same operating point predicted by the FE and DAE solver based model. It can be observed that the DAE solutions also match the FE prediction very well. It is also to be noted that the errors between the FE and DAE results arises from the coarse steps in i_f selected to generate the lookup table. A finer step size in the lookup tables will improve the model accuracy. The DAE based model is simpler to set up if a DAE solver, such as Saber, Modelica/Dymola, or Simulink/Simscape, etc, is available to the user compared to the ODE based solution which requires numerical inversion of the lookup tables. The numerical inversion with four variables can be time consuming and introduce additional errors in the model. A comparison of simulation time is shown in Table II where the time for numerical inversion to build the ODE based model is not included. It is evident that the proposed model dramatically reduces simulation time compared to FE analysis. It is worth noting that healthy machine FE simulation do not require as much time to solve as fault machine simulation, since the symmetry which can be employed in healthy conditions to reduce model size cannot be used in fault conditions, and the model has to be solved for several electrical cycles for the fault currents to reach a steady state.

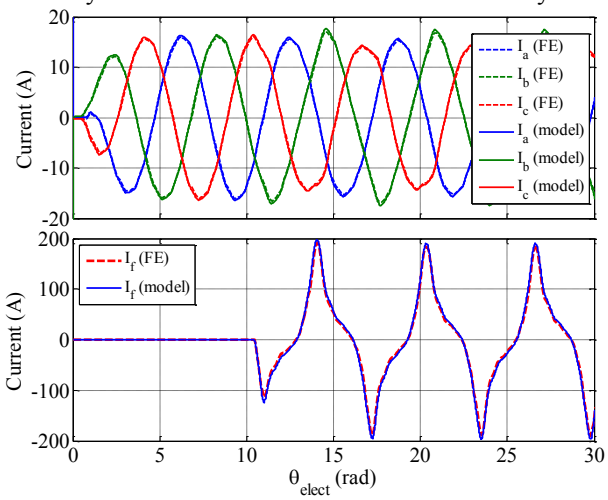

Fig. 9: Phase and fault current comparison of FE verses model (ODE) under transient condition at 3500 r/min. Step resistive load (2.2Ω) applied at θ_{elect}=0.5236 rad and 2 turn fault (R_f=5.5mΩ) at θ_{elect}=10.472 rad

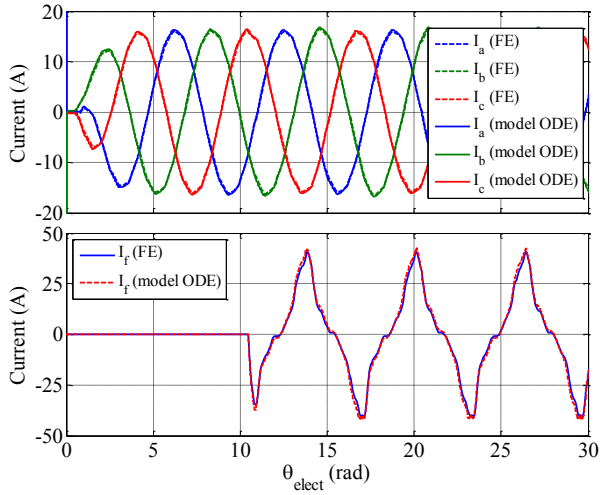

Fig. 10: Phase and fault current comparison of FE verses model (ODE) under transient condition at 3500 r/min with 10x nominal fault resistance (R_f =55mΩ). Step resistive load applied at θ_{elect}=0.5236 rad and 2 turn fault at θ_{elect}=10.472 rad.

Transient test is performed by introducing step load of 2.2Ω at θ_{elect}=0.5236 rad and 2 turn fault at θ_{elect}=10.472 rad at 3500 r/min, 2.2 ohm load as shown in Fig. 9. It can be observed that the model matches well with the FE prediction.

Effect of increase of fault resistance on model prediction is shown in Fig. 10 where the fault resistance is increased to 10 times the nominal value assumed in the simulations. It can be observed that there is a good match between FE and model predictions.

IV. Experimental Validation

A prototype 36s6p IPM machine whose specification is given in Table I was used for the purpose of validation of the fault model. The machine has 2 turns in C phase taken out of the machine for emulating the turn fault ($N_f = 2$). The machine winding and the fault turns are shown in Fig. 11. To test the system under fault, a 3 phase contactor connected to the faulted turns was triggered using a timer circuit to turn on for approximately 500ms. The time is deliberately kept small to prevent any damage to the coils due to prolonged circulating currents. Fig. 12 shows the experimental setup. The test machine is driven by a dynamometer and operates in generator mode connected to a 3 phase resistive load bank. Generator mode is chosen specifically to avoid any controller actions from a motor drive from affecting the validation of the faulted machine model. Moreover, creation of fault can cause inverter shutdown especially when fault currents are switched off by the fault timer circuit.

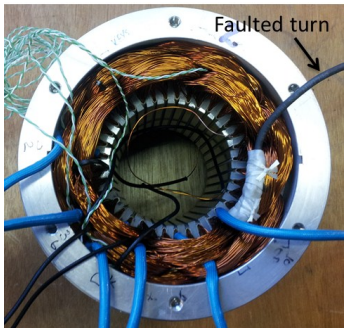

(a)

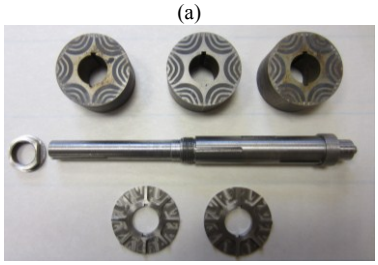

(b)

Fig. 11: (a)Stator winding with 2 turn fault in phase C (b) 3 step rotor and shaft

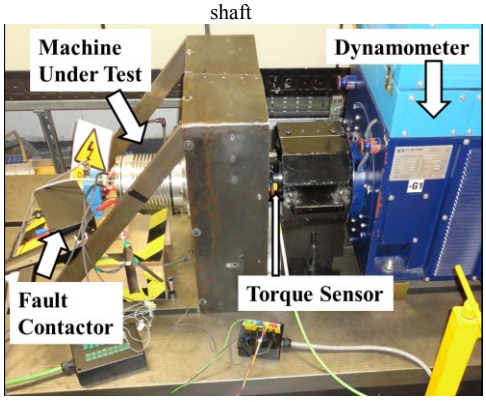

(a)

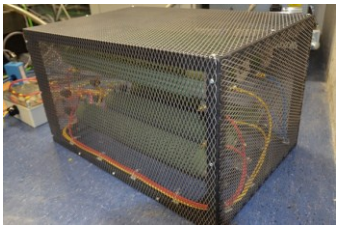

(b)

Fig. 12: Experimental Setup (a) Motor Dynamometer setup (b) Resistive load

First no load test under healthy condition was performed and the back-EMF noted and compared against model prediction. Fig. 13 shows the match between experiment and model.

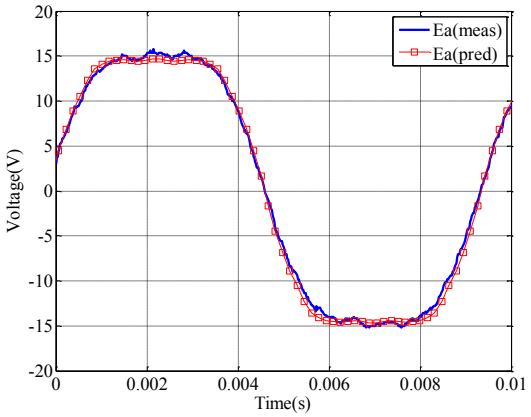

Fig. 13: Comparison of measured (meas) and FE model predicted (pred) phase back-EMF at 2100 r/min

The leakage inductance of the 2 turns was calculated to around 3.76μH. This however, does not account for the end-winding inductance and the inductance introduced due to external connection. When all these effects are accounted, the leakage inductance of the faulted turns was increased to 5.5μH. The contactor resistance was measured to be around 2-2.5mΩ. The extra connection wires from the winding to the contactor introduce an additional resistance of 3mΩ which was also accounted for in the model. To obtain positional alignment of the waveforms w.r.t to rotor position an analog sin/cos encoder was used. Fault tests were performed at four load conditions namely no-load, 1.01Ω, 2.2Ω, and 0.69Ω. For each load condition the speed of the machine is varied from 500r/min to 6500 r/min. Fig. 14 shows the comparison of measured and predicted peak and RMS fault current. It can be seen that there is a close match between experiments and simulation both in magnitude and overall trend of the graphs. The maximum error observed is about 20% and occurs at lower rotor speeds and lower load resistances. It is to be noted that in simulation the contactor resistance is accounted for at fixed value of 2mΩ. However, the contactor resistance has poor repeatability and varies from 2-2.5mΩ (25% variation) at different contactor closures during the experiments. At lower speeds, the resistive component dominates the overall fault impedance compared to higher speeds where dominating contributor is inductance. Consequently, the fault current is particularly sensitive to fault resistance variation at low speeds. It is therefore to be expected that the fault current

prediction could be less accurate at low speeds due to contactor resistance variation, and this should not be mistaken as inherent problem with model fidelity. It is also to be noted that FE modeling error, parasitic effects like the extra inductance introduced by the fault emulation set-up and machine construction on lamination BH characteristic all contributes to error. It is difficult to account all these effects in simulation accurately.

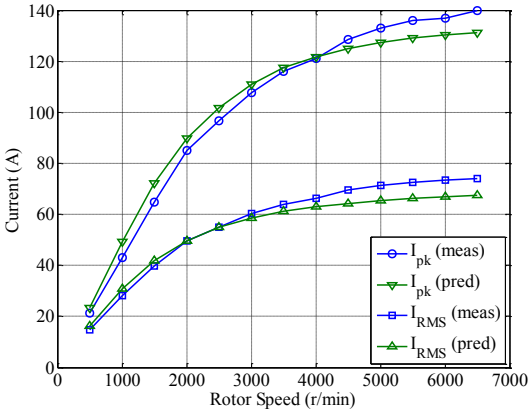

(a)

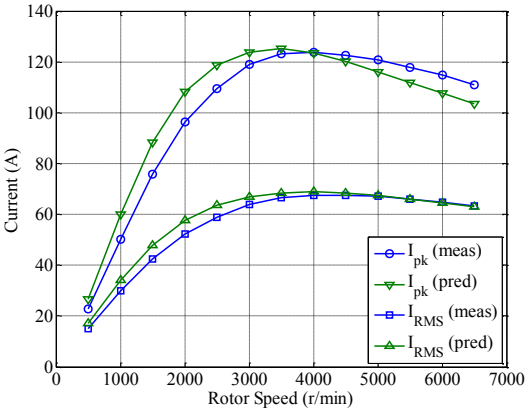

(b)

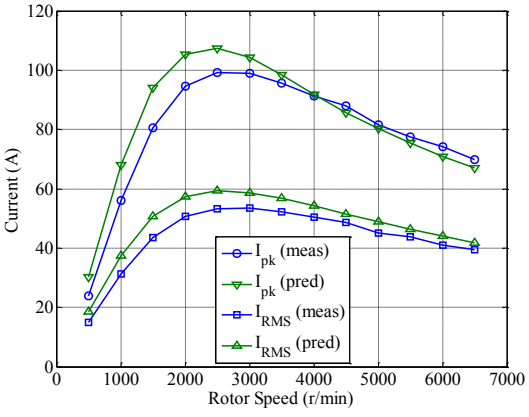

(c)

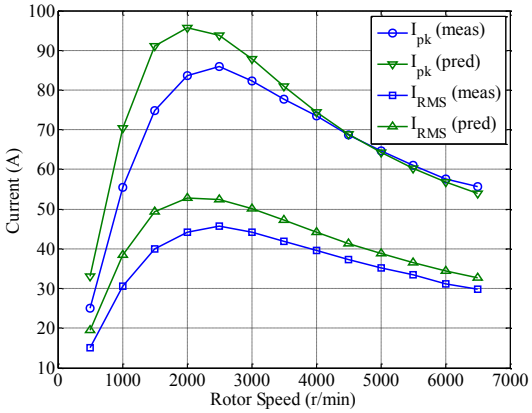

(d)

Fig. 14: Comparison of measured and predicted fault current variations with speed and load (a) No-load, (b) 2.2Ω load, (c) 1Ω load and (d) 0.69Ω load.

Measured and predicted instantaneous fault current waveforms are compared in Fig. 15 at 4 sample test-points at rotor speeds of 1500 r/min and 5500 r/min under no-load and at 0.69Ω load respectively. In all the 4 cases it can be observed that the predicted fault currents match well with the experimental waveforms in terms of both magnitude and shape. The differences are likely caused by the similar effects as described previously, namely, the parasitic inductance of the cables, uncertainty in contactor resistance and the effect of laser cutting on the magnetic property of the lamination which is not fully accounted in the FE model. Fig. 16 shows the performance of the model under a sample transient fault condition at 3500 r/min and 2.2Ω load.

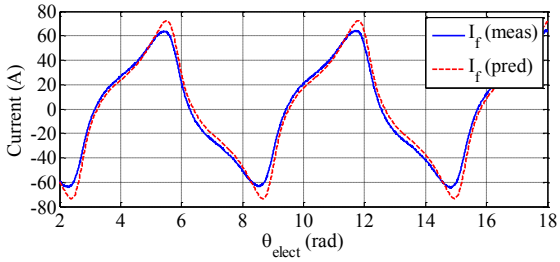

(a)

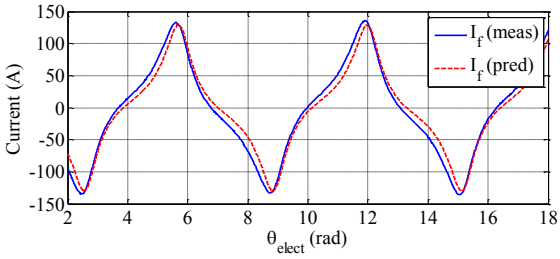

(b)

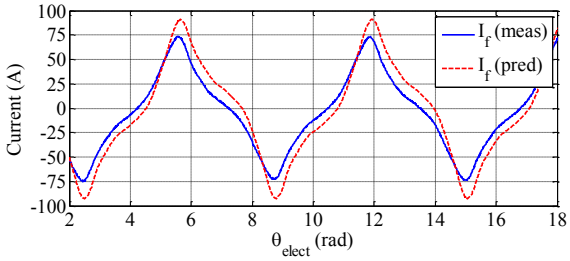

(c)

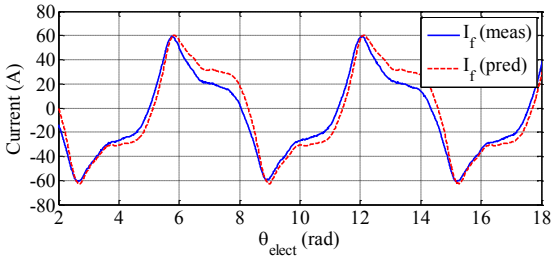

(d)

Fig. 15: Comparison of measured (meas) and predicted (pred) fault current at (a) 1500 r/min at no load, (b) 5500 r/min at no-load, (c) 1500 r/min at 0.69 Ω load and (d) 5500 r/min at 0.69 Ω load.

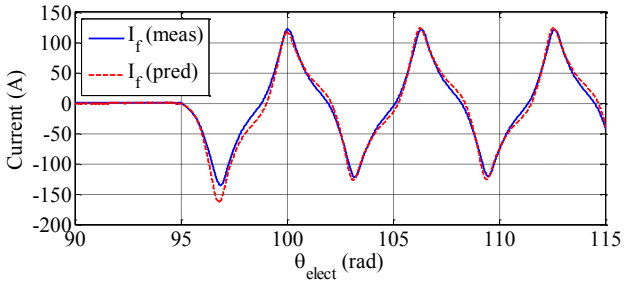

Fig. 16: Comparison of measured (meas) and predicted (pred) fault current (I_f) at 3500 r/min and 2.2Ω load. Turn fault initiated at $\theta_e = 95$ rad.

The inter-turn short-circuit fault will give rise to unbalance in the machine operation and hence additional current and voltage ripples. Measured and predicted i_d and i_q ripples are compared in Fig. 17 at 3 sample test-points at 5500 r/min with 2.2Ω load and 0.69Ω load, and at 3500 r/min with 2.2Ω load. It can be observed that the predicted ripple matches closely with experiment both in peak and wave-shape. It is to be noted that the voltage ripple is simply a scaled value of the current ripple since the machine is connected to a constant resistive load.

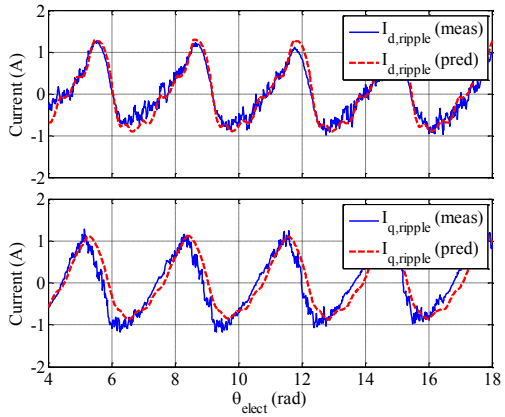

(a)

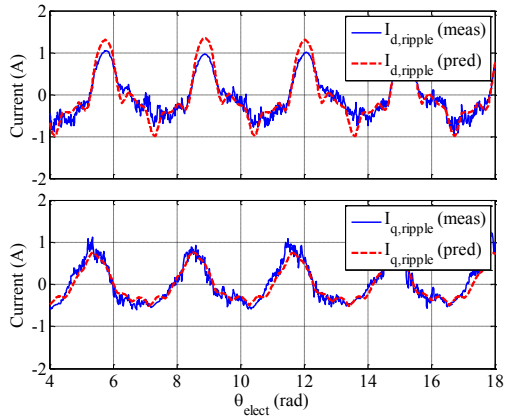

(b)

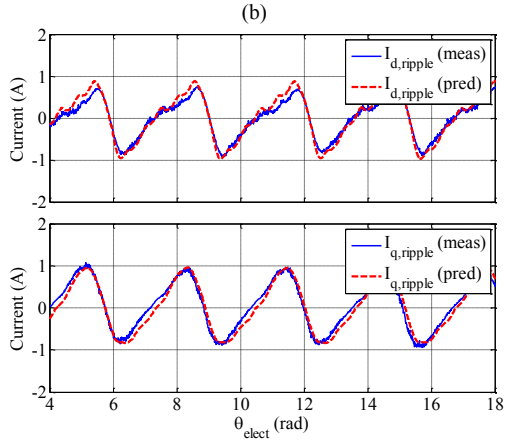

(c)

Fig. 17: Comparison of measured (meas) and predicted (pred) *dq* current ripple at (a) @5500 r/min and 2.2Ω load, (b) @5500 r/min and 0.69Ω load and (c) @3500 r/min and 2.2Ω load.

V. Conclusion

A methodology for derivation of detailed transient model of IPM machine under turn fault has been described. The effects of high level of saturation and rotor skew are accounted. It is shown through simulation and experiments that the model established with the proposed method is accurate and computationally efficient, and is able to capture the harmonics in the fault current and the dq currents in sufficient detail. The proposed modeling technique can also be used for modeling stator turn faults in other electrical machines including surface PM machines, switched reluctance machines, switched flux machines and wound field synchronous machines. The proposed model provides an effective tool for assessing inter-turn short-circuit fault behavior and for evaluation of associated fault detection techniques and mitigation strategies.

It should be noted that the effect of possible partial irreversible demagnetization as a result of inter-turn faults, and influence of temperature variation on permanent magnet field are not accounted in the model. These effects will be the subject of future research.

References

[1] Z. Q. Zhu and D. Howe, "Electrical Machines and Drives for Electric, Hybrid, and Fuel Cell Vehicles," *Proc. IEEE*, vol. 95, no. 4, pp. 746 – 765, Apr. 2007.

[2] K. T. Chau, C. C. Chan, and C. Liu, "Overview of Permanent-Magnet Brushless Drives for Electric and Hybrid Electric Vehicles," *IEEE Trans. Ind. Electron.*, vol. 55, no. 6, pp. 2246–2257, Jun. 2008.

[3] I. Boldea, L. N. Tutelea, L. Parsa, and D. Dorrell, "Automotive Electric Propulsion Systems With Reduced or No Permanent Magnets: An Overview," *IEEE Trans. Ind. Electron.*, vol. 61, no. 10, pp. 5696–5711, Oct. 2014.

[4] D. Dorrell, L. Parsa, and I. Boldea, "Automotive Electric Motors, Generators, and Actuator Drive Systems With Reduced or No Permanent Magnets and Innovative Design Concepts," *IEEE Trans. Ind. Electron.*, vol. 61, no. 10, pp. 5693–5695, Oct. 2014.

[5] K. Kamiev, J. Montonen, M. P. Ragavendra, J. Pyrhonen, J. A. Tapia, and M. Niemela, "Design Principles of Permanent Magnet Synchronous Machines for Parallel Hybrid or Traction Applications," *IEEE Trans. Ind. Electron.*, vol. 60, no. 11, pp. 4881–4890, Nov. 2013.

[6] P. Lazari, J. Wang, and L. Chen, "A Computationally Efficient Design Technique for Electric Vehicle Traction Machines," *IEEE Trans. Ind. Appl.*, vol. 50, no. 5, pp. 3203–3213, Oct. 2014.

[7] T. G. Habetler and Y. Lee, "Current-based condition monitoring and fault tolerant operation for electric machines in automotive applications," in *International Conference on Electrical Machines and Systems, 2007. ICEMS*, 2007, pp. 2011 –2016.

[8] B.-M. Ebrahimi and J. Faiz, "Feature Extraction for Short-Circuit Fault Detection in Permanent-Magnet Synchronous Motors Using Stator-Current Monitoring," *IEEE Trans. Power Electron.*, vol. 25, no. 10, pp. 2673–2682, 2010.

[9] J. A. Rosero, L. Romeral, J. A. Ortega, and E. Rosero, "Short-Circuit Detection by Means of Empirical Mode Decomposition and Wigner-Ville Distribution for PMSM Running Under Dynamic Condition," *IEEE Trans. Ind. Electron.*, vol. 56, no. 11, pp. 4534–4547, Nov. 2009.

[10] O. A. Mohammed, Z. Liu, S. Liu, and N. Y. Abed, "Internal Short Circuit Fault Diagnosis for PM Machines Using FE-Based Phase Variable Model and Wavelets Analysis," *IEEE Trans. Magn.*, vol. 43, no. 4, pp. 1729–1732, Apr. 2007.

[11] "Improved Motors for Utility Applications, Volume 1: Industry Assessment Study: Update and Analysis," EPRI, Technical Report EL-4286-V1, Oct. 1982.

[12] "Report of Large Motor Reliability Survey of Industrial and Commercial Installations, Part I," *IEEE Trans. Ind. Appl.*, vol. IA-21, no. 4, pp. 853–864, 1985.

[13] "Report of Large Motor Reliability Survey of Industrial and Commercial Installations, Part II," *IEEE Trans. Ind. Appl.*, vol. IA-21, no. 4, pp. 865–872, 1985.

[14] O. V. Thorsen and M. Dalva, "A survey of faults on induction motors in offshore oil industry, petrochemical industry, gas terminals, and oil refineries," *IEEE Trans. Ind. Appl.*, vol. 31, no. 5, pp. 1186–1196, 1995.

[15] A. H. Bonnett and C. Yung, "Increased Efficiency Versus Increased Reliability," *IEEE Ind. Appl. Mag.*, vol. 14, no. 1, pp. 29–36, 2008.

[16] Z. Sun, J. Wang, D. Howe, and G. Jewell, "Analytical Prediction of the Short-Circuit Current in Fault-Tolerant Permanent-Magnet Machines," *IEEE Trans. Ind. Electron.*, vol. 55, no. 12, pp. 4210 – 4217, Dec. 2008.

[17] A. H. Bonnett and G. C. Soukup, "Cause and analysis of stator and rotor failures in three-phase squirrel-cage induction motors," *IEEE Trans. Ind. Appl.*, vol. 28, no. 4, pp. 921–937, 1992.

[18] Y.-S. Lee, K.-T. Kim, and J. Hur, "Finite-Element Analysis of the Demagnetization of IPM-Type BLDC Motor With Stator Turn Fault," *IEEE Trans. Magn.*, vol. 50, no. 2, pp. 889–892, Feb. 2014.

[19] Y. Lee and T. G. Habetler, "A Phase Variable Simulation Model for Interior PM Synchronous Motor Drives with Stator Turn Faults," presented at the Power Electronics and Motion Control Conference, EPE-PEMC 2006, 2006, pp. 1074 –1079.

[20] R. M. Tallam, T. G. Habetler, and R. G. Harley, "Transient model for induction machines with stator winding turn faults," *IEEE Trans. Ind. Appl.*, vol. 38, no. 3, pp. 632–637, 2002.

[21] Y. Lee, "A Stator Turn Fault Detection Method and a Fault-Tolerant Operating Strategy for Interior PM Synchronous Motor Drives in Safety-Critical Applications," PhD Thesis, Georgia Institute of Technology, 2007.

[22] K.-T. Kim, J. Hur, B. Kim, and G.-H. Kang, "Circulating current calculation using fault modeling of IPM type BLDC motor of inter-turn fault," in *2011 International Conference on Electrical Machines and Systems (ICEMS)*, 2011, pp. 1 –5.

[23] M. Dai, A. Keyhani, and T. Sebastian, "Fault analysis of a PM brushless DC Motor using finite element method," *IEEE Trans. Energy Convers.*, vol. 20, no. 1, pp. 1 – 6, Mar. 2005.

[24] K.-T. Kim, J. Park, B. Kim, and J. Hur, "Comparison of the fault characteristics of IPM-type and SPM-type BLDC motors under Inter-Turn Faults conditions using Winding Function Theory," in *2012 IEEE Energy Conversion Congress and Exposition (ECCE)*, 2012, pp. 1262 –1269.

[25] K.-T. Kim, J.-K. Park, J. Hur, and B.-W. Kim, "Comparison of the Fault Characteristics of IPM-Type and SPM-Type BLDC Motors Under Inter-Turn Fault Conditions Using Winding Function Theory," *IEEE Trans. Ind. Appl.*, vol. 50, no. 2, pp. 986–994, Mar. 2014.

[26] N. Leboeuf, T. Boileau, B. Nahid-Mobarakeh, N. Takorabet, F. Meibody-Tabar, and G. Clerc, "Inductance Calculations in Permanent-Magnet Motors Under Fault Conditions," *IEEE Trans. Magn.*, vol. 48, no. 10, pp. 2605–2616, Oct. 2012.

[27] A. Sarikhani and O. A. Mohammed, "Inter-Turn Fault Detection in PM Synchronous Machines by Physics-Based Back Electromotive Force Estimation," *IEEE Trans. Ind. Electron.*, vol. 60, no. 8, pp. 3472–3484, Aug. 2013.

[28] T. J. E. Miller, M. Popescu, C. Cossar, and M. McGilp, "Performance estimation of interior permanent-magnet brushless motors using the voltage-driven flux-MMF diagram," *IEEE Trans. Magn.*, vol. 42, no. 7, pp. 1867–1872, Jul. 2006.

[29] X. Chen, J. Wang, B. Sen, P. Lazari, and T. Sun, "A High-Fidelity, Computationally Efficient Model for Interior Permanent Magnet Machines Considering the Magnetic Saturation, Spatial Harmonics and Iron Loss Effect," *IEEE Trans. Ind. Electron.*, vol. 62, no. 7, pp. 4044–4055, Jul. 2015.

[30] M. Boesing, M. Niessen, T. Lange, and R. De Doncker, "Modeling spatial harmonics and switching frequencies in PM synchronous machines and their electromagnetic forces," in *2012 XXth International Conference on Electrical Machines (ICEM)*, 2012, pp. 3001–3007.

[31] L. Chedot and G. Friedrich, "A cross saturation model for interior permanent magnet synchronous machine. Application to a starter-generator," in *Conference Record of the 2004 IEEE Industry Applications Conference, 2004. 39th IAS Annual Meeting*, 2004, vol. 1, p. 4 vol.(lvi+2822).

[32] N. Bianchi and S. Bolognani, "Magnetic models of saturated interior permanent magnet motors based on finite element analysis," in *The 1998 IEEE Industry Applications Conference, 1998. Thirty-Third IAS Annual Meeting*, 1998, vol. 1, pp. 27–34 vol.1.

[33] X. Chen, J. Wang, V. I. Patel, P. Lazari, L. Chen, and P. Lombard, "Reluctance Torque Evaluation for Interior Permanent Magnet Machines Using Frozen Permeability," in *7th IET International Conference on Power Electronics, Machines and Drives (PEMD 2014)*, Manchester, 2014, pp. 1–6.

[34] A. Sarikhani and O. A. Mohammed, "Inter-turn fault modeling of a variable speed pm wind generator using physics-based approach," in *Electric Machines Drives Conference (IEMDC), 2011 IEEE International*, 2011, pp. 636–641.

[35] S. Nadarajan, S. K. Panda, B. Bhangu, and A. K. Gupta, "Hybrid Model for Wound-Rotor Synchronous Generator to Detect and Diagnose Turn-to-Turn Short-Circuit Fault in Stator Windings," *IEEE Trans. Ind. Electron.*, vol. 62, no. 3, pp. 1888–1900, Mar. 2015.

[36] Y. Kano, K. Watanabe, T. Kosaka, and N. Matsui, "A Novel Approach for Circuit-Field-Coupled Time-Stepping Electromagnetic Analysis of Saturated Interior PM Motors," *IEEE Trans. Ind. Appl.*, vol. 45, no. 4, pp. 1325–1333, Jul. 2009.

[37] P. Lazari, B. Sen, J. Wang, and X. Chen, "Accurate d-q axis modelling of Synchronous Machines with Skew accounting for Saturation," presented at the IEEE International Magnetics Conference (INTERMAG - 2014), Dresden, 2014.

[38] E. Levi, "Saturation modelling in d-q axis models of salient pole synchronous machines," *IEEE Trans. Energy Convers.*, vol. 14, no. 1, pp. 44 –50, Mar. 1999.

[39] Paul C. Krause, Oleg Wasynczuk, Scott D. Sudhoff, Steven Pekarek, *Analysis of Electric Machinery and Drive Systems*, 3rd Edition. Wiley-IEEE Press.

[40] *Saber version 2011.09*. Synopsys, Mountain View, CA 94043: Synopsys, Inc., 2011.

[41] *MATLAB version 7.10.0*. Natick, Massachusetts: The MathWorks Inc., 2010.

[42] R. Siebert, J. Schneider, and E. Beyer, "Laser Cutting and Mechanical Cutting of Electrical Steels and its Effect on the Magnetic Properties," *IEEE Trans. Magn.*, vol. 50, no. 4, pp. 1–4, Apr. 2014.

Bhaskar Sen (S'11) received the B.E. degree from Delhi College of Engineering, Delhi, India in 2003 and the M.Tech. degree from Indian Institute of Technology, Kanpur, India in 2006. From 2006 to 2011, he was with GE Global Research, Bangalore, India. Since 2011 he has been working towards the Ph.D. degree in the University of Sheffield, UK. His current research interests include electrical machine fault modeling, machine fault detection and fault tolerant drives.

Jiabin Wang (SM'03) received the B.Eng. and M.Eng. degrees from Jiangsu University of Science and Technology, Zhengjiang, China, in 1982 and 1986, respectively, and the Ph.D. degree from the University of East London, London, U.K., in 1996, all in electrical and electronic engineering. Currently, he is a Professor in Electrical Engineering at the University of Sheffield, Sheffield, U.K. From 1986 to 1991, he was with the Department of Electrical Engineering at Jiangsu University of Science and Technology, where he was appointed a Lecturer in 1987 and an Associated Professor in 1990. He was a Postdoctoral Research Associate at the University of Sheffield, Sheffield, U.K., from 1996 to 1997, and a Senior Lecturer at the University of East London from 1998 to 2001. His research interests range from motion control and electromechanical energy conversion devices to electric drives for applications in automotive, renewable energy, household appliances and aerospace sectors.

Dr. Wang is a fellow of the Institute of Engineering and Technology, UK.

Panagiotis Lazari (S'13) was born in Limassol, Cyprus, in 1986. He received the B.Eng. degree in 2010 from the Department of Electronic and Electrical Engineering, The University of Sheffield, UK, where he is currently working towards the Ph.D. degree on the development of traction machines for EV applications.